Dalton Transactions

ROYAL SOCIETY OF CHEMISTRY

PAPER

View Article Online
View Journal | View Issue

Cite this: *Dalton Trans.*, 2023, **52**, 12892

Non-destructive food-quality analysis using near-infrared luminescence from $Mg_3Gd_2Ge_3O_{12}:Cr^{3+}$†

Chaojie Li,[a] Małgorzata Sójka,[b] Jiyou Zhong *[a] and Jakoah Brgoch *[b]

Rapid, non-destructive food-quality analysis using near-infrared (NIR) photoluminescence spectroscopy produced by phosphor-converted light-emitting diodes (pc-LEDs) has fascinating prospects for future food-safety monitoring. However, covering the energy window for organic molecular vibrations of interest in these applications requires NIR-emitting phosphors that are highly energy-efficient with ultra-broadband photoluminescence. This remains a materials design challenge. Here, a Cr^{3+}-substituted garnet phosphor, $Mg_3Gd_2Ge_3O_{12}$, is found to possess a desired broadband NIR emission (λ_{em} = 815 nm, fwhm = 172 nm; 2513 cm^{-1}) covering from 700 nm to 1200 nm with a photoluminescence quantum yield of 60.8% and absorption efficiency of 44.1% (λ_{ex} = 450 nm). Fabricating a prototype NIR pc-LED device using the title material combined with a 455 nm emitting InGaN LED chip produces a NIR output power of 23.2 mW with photoelectric efficiency of 8.45% under a 100 mA driving current. This NIR light source is then used to demonstrate the quantitative detection of ethanol in solution. These results highlight the feasibility of this material for NIR spectroscopy and validate the prospects of using NIR pc-LEDs in food-quality analysis.

Received 21st June 2023,
Accepted 22nd August 2023

DOI: 10.1039/d3dt01934a

rsc.li/dalton

1. Introduction

Near-infrared (NIR) spectroscopy is renowned for many remarkable traits such as deep tissue penetration, imperceptibility to human vision, and its ability to selectively absorb molecular vibrations of key organic functional groups (CH_3, NH_2, and OH).[1,2] As a result, it has gained significant interest across a wide array of fields, including food safety, medical diagnosis, modern agriculture, security and surveillance, and the realms of augmented reality (AR) and virtual reality (VR).[3–6] Traditional sources of NIR light primarily encompass, among others, tungsten halogen lamps and light-emitting diodes (LEDs). Unfortunately, the energy-efficiency of tungsten lamps is greatly diminished due to their suboptimal energy conversion, where a significant portion of the input energy is dissipated as heat rather than light. Direct NIR emitting LEDs like AlGaAs overcome this issue while also having prolonged operational lifespans and a generally more physically robust and compact design. Nonetheless, their emission consists of nearly monochromatic radiation with a narrow full width at half maximum (fwhm). This characteristic proves beneficial for applications like remote sensing, or optical fiber communications,[7,8] but it also imposes some constraints. For instance, when attempting to analyze the multiple vibrational signatures of organic molecules that span several thousand wavenumbers in energy, such as in food analysis, these limitations become apparent.

NIR phosphor-converted light-emitting diode (pc-NIR LED) technology is a promising alternative approach that offers the same advantages of the direct emitting NIR LEDs with the added potential for broad spectral coverage.[9–11] The current generation of pc-NIR LEDs combine a blue InGaN LED chip ($\lambda_{em} \approx 450$ nm) coated by a phosphor, which is an inorganic host material substituted with a luminescent ion that absorbs the LED's radiation and down-converts it into the desired NIR window. Considering the extensive effort that has already gone into optimizing the performance of blue-emitting LED chips, NIR light production is primarily limited by the phosphor's down-conversion process. Research has thus been dedicated to an in-depth investigation of the ions that can exhibit energy-efficient, broadband NIR photoluminescence. Usually, NIR luminescence is achieved through 4f ↔ 4f electronic transitions from rare-earth ions such as, Er^{3+}, Tm^{3+}, Nd^{3+} or Yb^{3+}.[12,13] However, the shielding of the 4f orbitals leads to very narrow fwhm values (>5 nm). Thus, down-conversion using these ions suffers from similar limits as direct NIR emitting LED chips. Conversely, transition metal ions like Ni^{2+}, Mn^{2+}, Cr^{3+}, or Fe^{3+} exhibit desired broadband luminescence.[14–17] Analyzing the optical properties of these transition metals

[a]School of Physics and Optoelectronic Engineering, Guangdong University of Technology, Guangzhou 510006, China. E-mail: zhongjiyou@126.com
[b]Department of Chemistry, University of Houston, Houston, Texas 77204, USA. E-mail: jbrgoch@uh.edu

† Electronic supplementary information (ESI) available. See DOI: https://doi.org/10.1039/d3dt01934a

show that Fe^{3+} and Ni^{2+} usually require UV or NIR excitation precluding their application with blue LED chips. Mn^{2+} emits in the visible part of the electromagnetic spectrum, making it useless for NIR applications.

The best option to make NIR emitting phosphors is arguably Cr^{3+}. This ion has been shown to not only have remarkable conversion efficiencies when excited by blue LED light, but tuning the crystal chemistry of the inorganic host also provides the ability to finely adjust the luminescence properties ($\lambda_{em,max}$, fwhm, *etc.*) while maintaining a high photoluminescence quantum yield (PLQY) within the NIR region.[18] As a result, numerous Cr^{3+}-substituted luminescent materials have been reported.[6,16,19–27] Research has focused specifically on identifying ways to achieving broadband Cr^{3+} NIR luminescence with nearly optimal PLQY values and robust optical properties as a function of temperature, which is determined based on the remaining emission intensity at 423 K (I_{423K}), an LED's approximate upper operating temperature.[21] Notably, garnet-type materials with the general formula $A_3B_2C_3O_{12}$ have been widely identified as highly efficient and thermally stable NIR phosphors. A few examples of these NIR emitters include: $Y_3In_2Ga_3O_{12}:Cr^{3+}$ (PLQY = 91.6%, I_{423K} = 100%), $Ca_3Sc_2Si_3O_{12}:Cr^{3+}$ (PLQY = 92.3%, I_{423K} = 97.4%), and $Gd_3In_2Ga_3O_{12}:Cr^{3+}$ (PLQY = 85.3%, I_{423K} = 87.7%).[22–24] The limit of these systems, however, is that the dense atomic arrangement intrinsic to garnets lead to increased crystal field splitting resulting in a blue-shifted emission spectrum occurring closer to the red portion of the visible spectrum, outside of the NIR window. Additionally, garnets high structural symmetry tend to result in a narrower fwhm and lower absorption coefficient due to Laporte forbidden nature of the octahedral 3d ↔ 3d transitions.[26]

Recently, our group has focused on designing NIR emitters based on Cr^{3+} that address some of these limitations. One method to maintain NIR luminescence in garnet-type materials is weakening the magnitude of crystal field splitting. As suggested in the $X_3Sc_2Ga_3O_{12}$ (X = Lu, Y, Gd, La) system,[27] moving from Lu^{3+} to progressively larger cations in the second coordination sphere like Y^{3+}, Gd^{3+}, La^{3+} will facilitate shift of the emission band towards longer wavelengths. As a result, some of the most exciting materials in this system are the Gd^{3+}-based garnet phosphors, which have shown an efficient NIR luminescence with PLQY values of ~55%. We have also helped establish that the co-occupation of ionic polyhedral subunits to increase lattice distortion is another effective way to red-shift the luminescence peak, while also increasing absorption efficiency and broadening the fwhm.[25,28] These changes are tremendously effective for creating efficient blue to NIR photon conversion using Cr^{3+}. Indeed, these ideas have been successfully applied to the creation of $Ga_{2-x}Mg_xGe_xO_3:Cr^{3+}$ and $Ca_3MgXGe_3O_{12}:Cr^{3+}$ (X = Zr, Hf, and Sn) based phosphors.[25,29]

In this work, we merge these design principles leading to the selection of $Mg_3Gd_2Ge_3O_{12}$ as a host structure for broadband, highly efficient NIR phosphor when substituted with Cr^{3+}. In this crystal structure, Mg^{2+} and Gd^{3+} are reported to co-occupy the dodecahedral crystallographic sites,[30] causing the desired local structure lattice distortions through a second-sphere interaction when Cr^{3+} is substituted on the Mg^{2+} octahedral site. The garnet structure-type maintains the overall NIR photoluminescence. The resulting emission is centered λ_{em} = 815 nm spans from 700 nm to 1200 nm (fwhm = 172 nm; 2513 cm^{-1}) when excited by 450 nm blue light. The ensuing PLQY (60.8%) and absorption efficiency (44.1%) measurements enable the fabrication of a prototype pc-NIR LED that produces an output power of 23.2 mW and photoelectric conversion efficiency of 8.45% under 100 mA driving current. This device is finally used to demonstrate the quantitative determination of alcohol concentration in samples, exhibiting remarkable accuracy and proof-of-concept for pc-NIR lighting as a source for monitoring molecular vibrations using ultra-compact handheld devices.

2. Experimental section

2.1 Synthesis

$Mg_{3-x}Gd_2Ge_3O_{12}:xCr^{3+}$ (x = 0, 0.01, 0.02, 0.04, 0.06, 0.08, and 0.10) garnet samples were synthesized by high-temperature solid-state reaction. First, $4MgCO_3{\cdot}Mg(OH)_2{\cdot}5H_2O$ (Macklin, 99.9%), Gd_2O_3 (Macklin, 99.99%), GeO_2 (Aladdin, 99.99%), and Cr_2O_3 (Aladdin, 99.99%) were used as the starting materials with an additional 5 wt% H_3BO_3 (Macklin, 99.99%) added as flux. The starting materials were thoroughly ground in an agate mortar and pestle for ≈40 minutes and then heated in a tube furnace at 1400 °C for 8 hours in air with heating and cooling rate of 3 °C min^{-1}. The final products were thoroughly ground into fine powders again with an agate mortar and pestle for subsequent measurements.

2.2 Characterization

The phase purity of each product was confirmed using powder X-ray diffraction obtained using the X'Pert3 PANalytical diffractometer (Cu Kα, λ = 1.5406 Å). Rietveld refinements of the diffractograms was performed using the General Structure Analysis System (GSAS) software and EXPGUI interface with a shifted Chebyshev function employed to describe the background.[31]

A UV-vis-NIR spectrophotometer (UV-3600 Plus, Shimadzu, Japan) was used to measure the diffuse reflectance (DR) spectra of these garnet samples. The room-temperature photoluminescence excitation, photoluminescence emission, temperature-dependent photoluminescence spectra and decay curves of the prepared samples were measured using the FLS-980 fluorescence spectrophotometer (Edinburgh Instruments), which equipped with a Xenon flash lamp (450 W, Osram) as the excitation source and an InGaAs detector. The photoluminescence quantum yield (PLQY) and absorption efficiency were determined on a Quantaurus-QY Plus C13534-11 (Hamamatsu Photonics) based on the integrating sphere with spectralon as a reference. The NIR pc-LED was fabricated by coating the optimized $Mg_{2.96}Gd_2Ge_3O_{12}:0.04Cr^{3+}$ phosphor

onto a 455 nm LED chip. The phosphor was adequately mixed with resin in a ratio of 1 : 1. The NIR photoelectric properties of the as-prepared pc-LED device were recorded using a HAAS2000 photoelectric measurement system (EVERFINE, China).

3. Results and discussion

3.1 Phase and crystal structure of Cr^{3+}-substituted $Mg_3Gd_2Ge_3O_{12}$

The crystal structure of the target product, $Mg_3Gd_2Ge_3O_{12}$, was first confirmed using the Rietveld method to analyze the powder X-ray diffractograms. The starting model was based on the reported $Mg_3Y_2Ge_3O_{12}$ garnet-type (PDF no. 89-6603) structure. The refinement, plotted in Fig. 1a, shows excellent agreement with this initial model supporting the phase purity of the product. The refined cell parameters and atomic positions are listed in Table 1 and Table S1,† respectively. The refined crystal structure of $Mg_3Gd_2Ge_3O_{12}$ is illustrated in Fig. 1b. The dodecahedral site occupancy includes statistical mixing between Gd^{3+} and Mg^{2+} ions (67%/33%) to match the originally reported mixed occupancy on the Wyckoff 24c site. The octahedral site is occupied exclusively by Mg^{2+} ions. Ge^{4+} occupies tetrahedral site within the garnet structure. Substituting Cr^{3+} into the structure following $Mg_{3-x}Gd_2Ge_3O_{12}$:xCr^{3+} (x = 0–0.10) indicates the structure is maintained based on the calculated diffractogram of the unsubstituted sample. The phase purity of the prepared phosphor samples is also verified (Fig. S1†). Subsequent structure refinements indicate the incorporation of Cr^{3+} causes the unit cell parameters (a, b, c) and cell volume (V) to decrease monotonically, As plotted in Fig. 1c and d. This change is attributed to the substitution of the smaller Cr^{3+} ion ($r_{6\text{-coor.}}$ = 0.615 Å) for the larger Mg^{2+} ion ($r_{6\text{-coor.}}$ = 0.72 Å) on the octahedral site.[32] The X-ray photoelectron spectroscopy (XPS), presented in Fig. 1d, further support the composition and valence state of the $Mg_{2.96}Gd_2Ge_3O_{12}$:$0.04Cr^{3+}$ sample. The signal with binding energies at 50 eV, 1219 eV, 32 eV, and 531 eV, is assigned to Mg-2p, Gd-3d, Ge-3d and O-1s, respectively; while a single signal peak corresponding to Cr-2p appears at 577 eV. These data indicate no other elements are present in the target product and that trivalent Cr is the main oxidation state of the activator ion in the sample.[33]

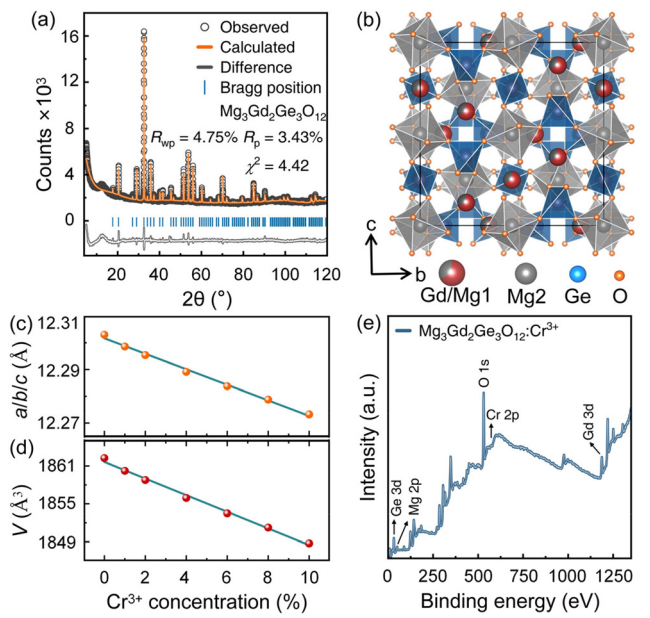

Fig. 1 (a) Rietveld refinement of XRD pattern for $Mg_3Gd_2Ge_3O_{12}$; (b) crystal structure of $Mg_3Gd_2Ge_3O_{12}$; (c and d) refined lattice parameters and unit cell volumes of $Mg_{3-x}Gd_2Ge_3O_{12}$:xCr^{3+} (x = 0–0.10) samples; (e) X-ray photoelectron spectroscopy (XPS) of $Mg_{2.96}Gd_2Ge_3O_{12}$:$0.04Cr^{3+}$ sample.

Table 1 Refined results of $Mg_3Gd_2Ge_3O_{12}$ garnet

Formula	$Mg_3Gd_2Ge_3O_{12}$
Radiation type; λ (Å)	X-ray; 1.5406
2θ (degree)	5–120
Temperature (K)	298
Space group	$Ia\bar{3}d$
$\alpha = \beta = \gamma$ (°)	90.00
$a = b = c$ (Å)	12.30301(7)
V (Å^3)	1862.23(7)
Profile R-factor, R_p	0.0343
Weighted profile R-factor, R_{wp}	0.0475
χ^2	4.42

3.2 Reflectivity and photoluminescence of $Mg_3Gd_2Ge_3O_{12}$:Cr^{3+}

The optical properties of the $Mg_3Gd_2Ge_3O_{12}$ host were first investigated by collecting the diffuse reflectance spectrum, provided in (Fig. S2†). The optical band gap of the host can be estimated by the following Kubelka–Munk formula in eqn (1) and (2),[34,35]

$$F(R) = \frac{(1-R)^2}{2R} \quad (1)$$

$$[F(R) \times h\nu]^{\frac{1}{n}} = A(h\nu - E_g) \quad (2)$$

where R represents the reflectance, $(1 - R)$ is the absorption, $h\nu$ is the photon energy, A is the absorption constant, and E_g is the value of optical band gap. The direct, allowed electronic transition in this garnet shows a band gap of 5.35 eV (for the unsubstituted host), significantly surpassing the host band gaps exhibited by numerous other Cr^{3+}-substituted phosphors, such as $Ca_3Sc_2Si_3O_{12}$ (E_g = 4.00 eV), $Y_3In_2Ga_3O_{12}$ (E_g = 4.98 eV), and $Na_3In_2Li_3F_{12}$ (E_g = 5.30 eV).[23,36,37] The wide bandgap is advantageous because it limits thermally-activated photoionization-induced thermal quenching processes, which increase the probability of non-radiative transitions that shut down photoluminescence.

Plotting the normalized excitation and diffuse reflectance (orange dotted line) spectra of $Mg_{2.96}Gd_2Ge_3O_{12}$:$0.04Cr^{3+}$ (Fig. 2a) shows two broad excitation/absorption bands located in the blue region (452 nm) and red region (637 nm) that can

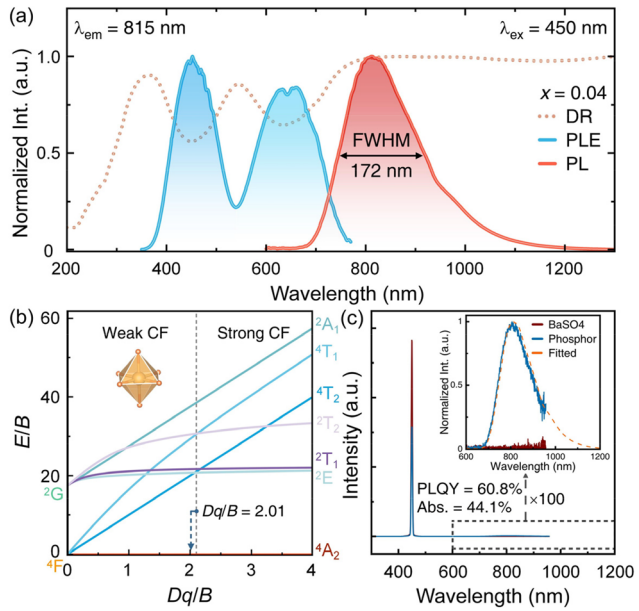

Fig. 2 (a) DR (orange dotted line), PLE (blue), and PL (red) spectra of $Mg_{2.96}Gd_2Ge_3O_{12}$:0.04Cr^{3+} phosphor excited by 450 nm radiation and monitored at 815 nm wavelength; (b) Tanabe–Sugano diagram for Cr^{3+} ion in octahedral crystal field; (c) photoluminescence quantum yield and absorption efficiency of $Mg_{2.96}Gd_2Ge_3O_{12}$:0.04Cr^{3+} phosphor excited by 450 nm.

be assigned to the $^4A_2 \rightarrow {}^4T_1$ (^4F) and $^4A_2 \rightarrow {}^4T_2$ (^4F) electronic transitions of Cr^{3+}, respectively.[38] Upon 450 nm excitation, a broadband NIR photoluminescence emission peak appears centered λ_{max} = 815 nm and spanning from 700 nm to 1200 nm with a fwhm of 172 nm (2513 cm^{-1}). This emission can be attributed to the $^4T_2$ (^4F) $\rightarrow$ $^4A_2$ transition of Cr^{3+} in weak octahedral crystal field. This can be further understood following Tanabe–Sugano theory, where the crystal field splitting (D_q) and the Racah parameter (B) of Cr^{3+} are used to determine the crystal field strength by the following eqn (3) and (4),[39,40]

$$10D_q = E(^4A_2 \rightarrow {}^4T_2) - \Delta S/2 \quad (3)$$

$$D_q/B = \frac{15(m-8)}{m^2-10m} \quad (4)$$

$$m = \frac{E(^4A_2 \rightarrow {}^4T_1) - E(^4A_2 \rightarrow {}^4T_2)}{D_q} \quad (5)$$

where $E(^4A_2 \rightarrow {}^4T_1)$ and $E(^4A_2 \rightarrow {}^4T_2)$ are obtained from the peak positions of excitation bands corresponding to the $^4T_1$ and $^4T_2$ levels and ΔS represents the Stokes shift. The values of D_q and B were calculated to 1399 cm^{-1} and 696 cm^{-1}, respectively, while D_q/B value found to be 2.01 (<2.3) (shown in Fig. 2b). This suggests that the compound falls on the limit of weak crystal field splitting for Cr^{3+}. Given value is lower than for other reported Cr^{3+} substituted-garnet phosphors as $Gd_3Sc_{1.47}Al_{0.5}Ga_3O_{12}$:$Cr^{3+}$ ($D_q/B \approx 2.53$, $\lambda_{em,max}$ = 638 nm),[22] $Y_3In_2Ga_3O_{12}$:Cr^{3+} ($D_q/B \approx 2.24$, $\lambda_{em,max}$ = 760 nm),[23] or $Ca_3Sc_2Si_3O_{12}$:Cr^{3+} (D_q/B = 2.22, $\lambda_{em,max}$ = 770 nm)[24] resulting in a shifting emission towards lower wavelengths ($\lambda_{em,max}$ = 815 nm).

The excitation and emission spectra of $Mg_3Gd_2Ge_3O_{12}$:Cr^{3+} with various Cr^{3+} concentrations are shown in Fig. S3(a and b).† The excitation spectra remain relatively unaltered across the entire range, the peak position of emission spectra gradually shifts from 800 nm to 830 nm as the Cr^{3+} concentration increases. Although the red-shift of the emission spectra seems to be counter to conventional crystal filed theory following a contraction of the unit cell parameters upon Cr^{3+} substitution, the concurrent spectral reabsorption, Stokes shift, and energy transfer are instead likely to induce the observed red-shift.[41] Additionally, along with the observed red shift, increasing the Cr^{3+} concentration is associated with a slight broadening of the emission peak (fwhm ≈ 10 nm; 55 cm^{-1}) stemming from additional local structural distortions that are occurring with the induced site disorder.

As the Cr^{3+} substitution exceeds x = 0.04, concentration quenching occurs (as plotted in Fig. S4†). The optimal photoluminescence quantum yield (PLQY) and absorption efficiency of the optimized $Mg_{2.96}Gd_2Ge_3O_{12}$:0.04Cr^{3+} sample under the 450 nm excitation are determined to reach 60.8% and 44.1%, respectively (Fig. 2c). The PLQY value is reasonable compared to other NIR emitting garnet materials with emission wavelength longer than 810 nm (listed in Table 2), such as $La_3Sc_2Ga_3O_{12}$:Cr^{3+} (PLQY = 35%), $Ca_2LaZr_2Ga_{2.8}Al_{0.2}O_{12}$:$Cr^{3+}$ (PLQY = 58.3%), and $Ca_4ZrGe_3O_{12}$:Cr^{3+} (PLQY = 35%).[27,42,43] Room-temperature photoluminescence decay curves of $Mg_{3-x}Gd_2Ge_3O_{12}$:xCr^{3+} (x = 0, 0.01, 0.02, 0.04, 0.06, 0.08, and 0.10) were also measured and are presented in Fig. S5(a–f).† The decay curves can be described by a single-exponential function corroborating one crystallographic position for Cr^{3+} in the investigated garnet. The fitting function is described by eqn (6),[44]

$$I_t = I_0 \exp\left(-\frac{t}{\tau}\right) \quad (6)$$

where I_0 and I_t represent the emission intensity at time 0 and t; τ represents calculated lifetime. As the Cr^{3+} doping concentration increases, the lifetime decreases gradually from 40.11 μs to 26.96 μs going from x = 0.01 to x = 0.10. This further supports increasing probability of non-radiative relaxation due to concentration quenching.

3.3 Thermal stability of $Mg_3Gd_2Ge_3O_{12}$:Cr^{3+}

InGaN blue LEDs generate elevated temperatures as high as ≈423 K during normal operation. Thus, it is imperative to investigate thermal stability of $Mg_{2.96}Gd_2Ge_3O_{12}$:0.04Cr^{3+}. Fig. 3a presents the contour plot of temperature-dependent emission spectra recorded from 298 K to 473 K when excited at 450 nm. Fig. S6† shows the raw data. Increasing temperature causes the emission spectrum to undergo a subtle red-shift attributed to the thermally induced expansion of the crystal structure, while the concurrent broadening can be directly

Table 2 Photoluminescence properties of Cr^{3+}-activated broadband garnet phosphors

Phosphor	λ_{em}	PLQY	Abs.	EQE	I_{423K}	fwhm	Ref.
$Mg_3Gd_2Ge_3O_{12}:Cr^{3+}$	815 nm	60.8%	44.1%	26.8%	44.5%	172 nm	This work
$CaLu_2Mg_2Si_3O_{12}:Cr^{3+}$	750 nm	85.7%	45.0%	38.6%	≈95%	≈100 nm	51
$Y_3In_2Ga_3O_{12}:Cr^{3+}$	760 nm	91.6%	46.6%	42.7%	100%	125 nm	23
$Ca_3Sc_2Si_3O_{12}:Cr^{3+}$	770 nm	92.3%	≈27.6%	25.5%	97.4%	100 nm	24
$Na_3In_2Li_3F_{12}:Cr^{3+}$	778 nm	87.2%	≈ 23%	20.05%	58%	121 nm	37
$Gd_3In_2Ga_3O_{12}:Cr^{3+}$	780 nm	85.3%	49.1%	41.9%	87.8%	124 nm	52
$Lu_2CaMg_2Ge_3O_{12}:Cr^{3+}$	795 nm	57.8%	46.3%	26.8%	67.1%	152 nm	53
$Ca_3MgHfGe_3O_{12}:0.02Cr^{3+}$	800 nm	90.7%	27.8%	25.2%	84.5%	125 nm	25
$Gd_3Zn_{0.8}Ga_{3.4}Ge_{0.8}O_{12}:Cr^{3+}$	800 nm	79.6%	≈39.2%	31.2%	40.2%	202 nm	54
$La_3Sc_2Ga_3O_{12}:Cr^{3+}$	818 nm	35%	—	—	—	145 nm	27
$Ca_2LaZr_2Ga_{2.8}Al_{0.2}O_{12}:Cr^{3+}$	820 nm	58.3%	≈40.3%	23.5%	≈64%	160 nm	42
$Ca_4ZrGe_3O_{12}:Cr^{3+}$	840 nm	35%	—	—	—	160 nm	43

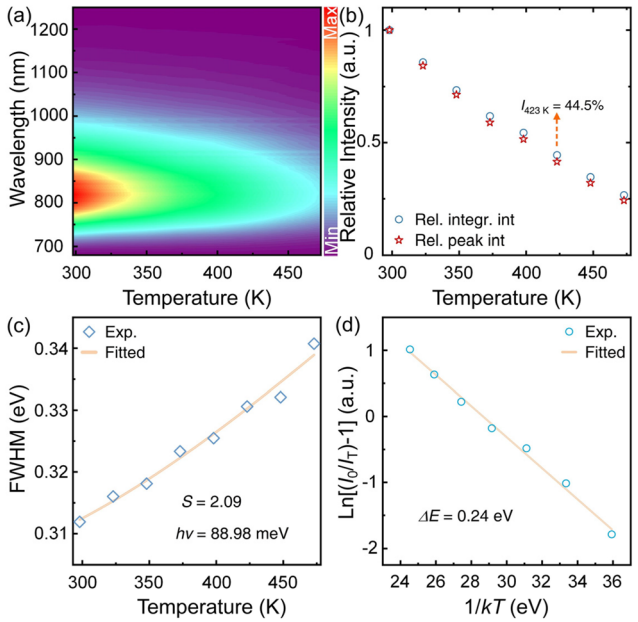

Fig. 3 (a) Contour plot of the temperature-dependent emission spectra, and (b) relative integral and peak intensity of $Mg_{2.96}Gd_2Ge_3O_{12}:0.04Cr^{3+}$ phosphor excited by 450 nm; (c) fitted Huang–Rhys factor (S) and the phonon energy (hv); (d) fitting the relationship between $\ln[(I_0/I_T) - 1]$ *versus* $1/kT$.

linked to changes in magnitude of the electron–phonon coupling.[25,45] Once the temperature increases to 423 K, the integrated emission intensity drops to only 44.5% of the room temperature emission intensity (as plotted in Fig. 3b).

Considering the wide bandgap of the host material, luminescence quenching through thermally activated photoionization seems to be fairly unlikely.[25] The more likely mechanism of quenching in this material is due to potential energy surface cross-over. This involves a shift between the excited state potential energy surface relative to the ground state energy surface. If this shift is large then quenching becomes possible. Typically, in Cr^{3+}-substituted materials high-energy phonons cause loss of the emission intensity at high temperature due to the non-radiative transitions caused by phonon-induced relaxation at the crossover point of the $^4A_2$ and $^4T_2$ ground and excited parabolas, respectively.[46,47] Therefore, to investigate cross-over mechanism it becomes imperative to determine parabolas offset, which governs the magnitude electron–phonon coupling in given material and can be characterized by Huang–Rhys factor (S). Experimentally, S can be extracted by measuring fwhm of the Cr^{3+}-substituted phosphor emission band as a function of temperature. The value of S can then be calculated according to eqn (7),[48,49]

$$\text{fwhm}\,(T) = \sqrt{8 \times \ln 2} \times \sqrt{S} \times hv \times \sqrt{\coth \frac{hv}{2 \times k_B \times T}} \quad (7)$$

where hv is the photon energy, and k_B is the Boltzmann's constant. As shown in Fig. 3c, S and hv are determined to be 2.09 meV and 88.98 meV, respectively, from the fitting. This value of S is lower than Cr^{3+}-substituted materials like $KGaP_2O_7:Cr^{3+}$ (S = 2.21), $GaTaO_4:Cr^{3+}$ (S = 3.82), and $Ca_3Sc_2Si_3O_{12}:Cr^{3+}$ (S = 4.0).[19,20,24] However, it is still a reasonably large S, which combined with the likely structural distortion can cause a significant reduction of S value, which has also been reported.[28] An energy barrier for thermal quenching induced by cross-over process can also be calculated. The activation energy responsible for the thermal quenching, ΔE, can be determined following by the Arrhenius equation (eqn (8)),[50]

$$I_T = \frac{I_0}{1 + C\exp(-\Delta E/kT)} \quad (8)$$

where I_0 and I_T represent emission intensity at temperature 298 K and T, respectively; C is the constant. The resulting value of ΔE that is responsible for quenching process is estimated to be 0.24 eV (Fig. 3d). This is a relatively low energy barrier suggesting a high probability of thermal quenching at elevated temperature under normal circumstances further supporting the relatively big drop off in emission intensity at elevated temperature. Improving this material will require identifying ways to chemically alter the phosphor to increase this cross-over activation barrier.

3.4 Prototype device fabrication and the quantitative detection of ethanol in solution

To evaluate the practical viability of the $Mg_3Gd_2Ge_3O_{12}:Cr^{3+}$ phosphor for non-destructive food analysis, a prototype NIR

pc-LED device was fabricated by coating the optimal sample on a blue InGaN LED chip (455 nm). The device is presented in the inset of Fig. 4a. The emission spectra were measured as a function of the driving current from 25 mA to 350 mA, as shown in Fig. 4a. As the driving current increases the NIR output power gradually increases. Although the photoelectric efficiency decreases, this is mostly due to a drop in LED chip efficiency (Table S2†) rather than a change in the phosphor. The pc-LED device at 100 mA current exhibits a NIR output power of 23.24 mW and photoelectric efficiency of 8.45%. This is a sufficient balance of output power and efficiency for use in qualitative as well as quantitative molecular vibrational analysis. Considering the luminescence from Cr^{3+} in this host nicely overlaps with the overtones and vibrations of the O–H, C–H and N–H bonds, the fabricated pc-NIR LED was used as the light source to monitor the change in a NIR transmission spectrum.[55]

Placing a cuvette containing an alcohol solution into the optical path of the sample chamber of the spectrometer using the prototype pc-NIR LED as the excitation source, the transmission spectra for different alcohol concentrations was collected, illustrated in Fig. S7.† Collecting the absorption spectra (Fig. 4c) clearly displays that the characteristic absorption around 908 nm and 970 nm, which can be assigned to the absorption of different vibrational modes of C–H and O–H bonds, respectively, change as a function of concentration. Analyzing the intensity of the transmission confirms signal intensity at these two positions shows a linear correlation with alcohol concentration (Fig. 4d). These results highlight that the $Mg_3Gd_2Ge_3O_{12}:Cr^{3+}$ phosphor has potential in spectroscopy applications.

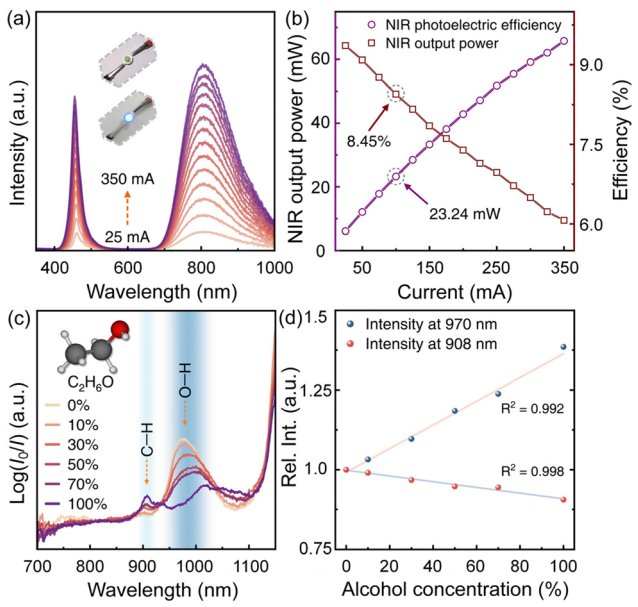

Fig. 4 (a) Electroluminescence spectra of NIR pc-LED device under different driving currents (25 mA–350 mA). The insets show a fabricated device with (up) and without (below) LED on; (b) NIR output power, and NIR photoelectric conversion efficiency of the fabricated NIR pc-LED device; (c) calculated absorption spectra of the alcohol in various concentrations; (d) relationships between intensity ratio (at 908 nm and 970 nm) and alcohol concentrations.

4. Conclusion

In summary, this work presents a Cr^{3+}-activated garnet phosphor with broadband long-wavelength NIR emission selected based on its mixed crystallographic occupancy within the family of garnet-type host materials. In the crystal structure, $Mg_3Gd_2Ge_3O_{12}$, [Gd^{3+}–Mg^{2+}] ionic units co-occupy the dodecahedral sites causing local distortions can lead to the spectral red-shift. After substitution of Cr^{3+} into host structure, the phosphor exhibits a broadband NIR emission covering the range from 700 nm to 1200 nm, with an λ_{em} = 815 nm and an fwhm of 172 nm when excited by 450 nm blue light. Optimal Cr^{3+} doping concentration is 4 mol% with an internal PLQY and absorption efficiency reach 60.8% and 44.1%, respectively. The emission intensity at 423 K maintains 44.5% of the initial emission intensity. Moreover, fabricating an NIR pc-LED device by using the optimized sample combining with a 455 nm LED chip produces a functional prototype that can be used to quantitively measure the vibrational spectra of alcohol solutions *via* monitoring around ≈908 nm and ≈970 nm. These results indicate that the $Mg_3Gd_2Ge_3O_{12}:Cr^{3+}$ phosphor not only demonstrates a great potential in NIR pc-LED applications, but also provides exceptional reference for the design of garnet-type phosphors.

Conflicts of interest

The authors declare no competing financial interest.

Acknowledgements

The authors (C. L. and J. Z.) thank the Guangzhou Basic and Applied Basic Research Project (202201010689) and the Analysis and Test Center of Guangdong University of Technology. The authors (M. S. and J. B.) also thank the U.S. National Science Foundation (DMR-1847701).

References

1 C. Rogel-Castillo, R. Boulton, A. Opastpongkarn, G. Huang and A. E. Mitchell, *J. Agric. Food Chem.*, 2016, **64**, 5958–5962.
2 G. Liu, T. Hu, M. S. Molokeev and Z. Xia, *iScience*, 2021, **24**, 102250.
3 F. Vatansever and M. R. Hamblin, *Photonics Lasers Med.*, 2012, **1**, 255–266.
4 A. A. Lucero, G. Addae, W. Lawrence, B. Neway, D. P. Credeur, J. Faulkner, D. Rowlands and L. Stoner, *Exp. Physiol.*, 2018, **103**, 90–100.

5 M. Manley, *Chem. Soc. Rev.*, 2014, **43**, 8200–8214.
6 M. H. Fang, G. N. A. De Guzman, Z. Bao, N. Majewska, S. Mahlik, M. Grinberg, G. Leniec, S. M. Kaczmarek, C. W. Yang, K. M. Lu, H. S. Sheu, S. F. Hu and R. S. Liu, *J. Mater. Chem. C*, 2020, **8**, 11013–11017.
7 M. Vasilopoulou, A. Fakharuddin, F. P. García de Arquer, D. G. Georgiadou, H. Kim, A. R. bin Mohd Yusoff, F. Gao, M. K. Nazeeruddin, H. J. Bolink and E. H. Sargent, *Nat. Photonics*, 2021, **15**, 656–669.
8 K. Guo, M. Righetto, A. Minotto, A. Zampetti and F. Cacialli, *iScience*, 2021, **24**, 102545.
9 V. Rajendran, T. Lesniewski, S. Mahlik, M. Grinberg, G. Leniec, S. M. Kaczmarek, W. K. Pang, Y. S. Lin, K. M. Lu, C. M. Lin, H. Chang, S. F. Hu and R. S. Liu, *ACS Photonics*, 2019, **6**, 3215–3224.
10 G. Liu, M. S. Molokeev and Z. Xia, *Chem. Mater.*, 2022, **34**, 1376–1384.
11 G. Liu and Z. Xia, *J. Phys. Chem. Lett.*, 2022, **13**, 5001–5008.
12 L. Kong, Y. Liu, L. Dong, L. Zhang, L. Qiao, W. Wang and H. You, *Dalton Trans.*, 2020, **49**, 8791–8798.
13 S. Nishimura, S. Fuchi and Y. Takeda, *J. Mater. Sci.: Mater. Electron.*, 2017, **28**, 7157–7162.
14 L. Yuan, Y. Jin, H. Wu, K. Deng, B. Qu, L. Chen, Y. Hu and R.-S. Liu, *ACS Appl. Mater. Interfaces*, 2022, **14**, 4265–4275.
15 S. Adachi, *J. Lumin.*, 2018, **202**, 263–281.
16 H. Zeng, T. Zhou, L. Wang and R. J. Xie, *Chem. Mater.*, 2019, **31**, 5245–5253.
17 D. Liu, G. Li, P. Dang, Q. Zhang, Y. Wei, L. Qiu, M. S. Molokeev, H. Lian, M. Shang and J. Lin, *Light: Sci. Appl.*, 2022, **11**, 112.
18 M. Sójka, J. Zhong and J. Brgoch, *ACS Appl. Opt. Mater.*, 2023, **1**, 1138–1149.
19 J. Zhong, Y. Zhuo, F. Du, H. Zhang, W. Zhao, S. You and J. Brgoch, *Adv. Opt. Mater.*, 2022, **10**, 2101800.
20 J. Zhong, C. Li, W. Zhao, S. You and J. Brgoch, *Chem. Mater.*, 2022, **34**, 337–344.
21 P. Dang, Y. Wei, D. Liu, G. Li and J. Lin, *Adv. Opt. Mater.*, 2023, **11**, 2201739.
22 E. T. Basore, W. Xiao, X. Liu, J. Wu and J. Qiu, *Adv. Opt. Mater.*, 2020, **8**, 2000296.
23 C. Li and J. Zhong, *Chem. Mater.*, 2022, **34**, 8418–8426.
24 Z. Jia, C. Yuan, Y. Liu, X.-J. Wang, P. Sun, L. Wang, H. Jiang and J. Jiang, *Light: Sci. Appl.*, 2020, **9**, 86.
25 C. Li and J. Zhong, *Adv. Opt. Mater.*, 2023, **11**, 2202323.
26 F. Zhao, Z. Song and Q. Liu, *Laser Photonics Rev.*, 2022, **16**, 2200380.
27 B. Malysa, A. Meijerink and T. Jüstel, *J. Lumin.*, 2018, **202**, 523–531.
28 Z. Liao, J. Zhong, C. Li, H. Jiang and W. Zhao, *Phys. Chem. Chem. Phys.*, 2023, **25**, 15452–15462.
29 J. Zhong, L. Zeng, W. Zhao and J. Brgoch, *ACS Appl. Mater. Interfaces*, 2022, **14**, 51157–51164.
30 S. Geller, C. E. Miller and R. G. Treuting, *Acta Crystallogr.*, 1960, **13**, 179–186.
31 B. H. Toby and R. B. Von Dreele, *J. Appl. Crystallogr.*, 2013, **46**, 544–549.
32 R. D. Shannon, *Acta Crystallogr., Sect. A: Cryst. Phys., Diffr., Theor. Gen. Crystallogr.*, 1976, **32**, 751–767.
33 A. Kadari, T. Schemme, D. Kadri and J. Wollschläger, *Results Phys.*, 2017, **7**, 3124–3129.
34 A. Mondal, S. Das and J. Manam, *RSC Adv.*, 2016, **6**, 82484–82495.
35 P. Makuła, M. Pacia and W. Macyk, *J. Phys. Chem. Lett.*, 2018, **9**, 6814–6817.
36 Y. Zhou, X. Li, T. Seto and Y. Wang, *ACS Sustainable Chem. Eng.*, 2021, **9**, 3145–3156.
37 W. Nie, Y. Li, J. Zuo, Y. Kong, W. Zou, G. Chen, J. Peng, F. Du, L. Han and X. Ye, *J. Mater. Chem. C*, 2021, **9**, 15230–15241.
38 H. Zhang, J. Zhong, F. Du, L. Chen, X. Zhang, Z. Mu and W. Zhao, *ACS Appl. Mater. Interfaces*, 2022, **14**, 11663–11671.
39 Y. Tanabe and S. Sugano, *J. Phys. Soc. Jpn.*, 1954, **9**, 766–779.
40 A. Trueba, P. Garcia-Fernandez, J. M. García-Lastra, J. A. Aramburu, M. T. Barriuso and M. Moreno, *J. Phys. Chem. A*, 2011, **115**, 1423–1432.
41 X. Liu, Z. Song, Y. Kong, S. Wang, S. Zhang, Z. Xia and Q. Liu, *J. Alloys Compd.*, 2019, **770**, 1069–1077.
42 Y. Liu, S. He, D. Wu, X. Dong and W. Zhou, *ACS Appl. Electron. Mater.*, 2022, **4**, 643–650.
43 J. Xiang, J. Zheng, X. Zhao, X. Zhou, C. Chen, M. Jin and C. Guo, *Mater. Chem. Front.*, 2022, **6**, 440–449.
44 M.-H. Fang, K.-C. Chen, N. Majewska, T. Leśniewski, S. Mahlik, G. Leniec, S. M. Kaczmarek, C.-W. Yang, K.-M. Lu, H.-S. Sheu and R.-S. Liu, *ACS Energy Lett.*, 2021, **6**, 109–114.
45 X. Xu, Q. Shao, L. Yao, Y. Dong and J. Jiang, *Chem. Eng. J.*, 2020, **383**, 123108.
46 J. Zhong, Y. Zhuo, F. Du, H. Zhang, W. Zhao and J. Brgoch, *ACS Appl. Mater. Interfaces*, 2021, **13**, 31835–31842.
47 P. Dorenbos, *J. Phys.: Condens. Matter*, 2005, **17**, 8103–8111.
48 J. H. Ryu, H. S. Won, Y. G. Park, S. H. Kim, W. Y. Song, H. Suzuki and C. Yoon, *Appl. Phys. A: Mater. Sci. Process.*, 2009, **95**, 747–752.
49 C. Liu, Z. Qi, C.-G. Ma, P. Dorenbos, D. Hou, S. Zhang, X. Kuang, J. Zhang and H. Liang, *Chem. Mater.*, 2014, **26**, 3709–3715.
50 X. Ji, J. Zhang, Y. Li, S. Liao, X. Zhang, Z. Yang, Z. Wang, Z. Qiu, W. Zhou, L. Yu and S. Lian, *Chem. Mater.*, 2018, **30**, 5137–5147.
51 H. Xiao, J. Zhang, L. Zhang, H. Wu, H. Wu, G. Pan, F. Liu and J. Zhang, *Adv. Opt. Mater.*, 2021, **9**, 2101134.
52 C. Li, J. Zhong, H. Jiang and P. Shi, *Dalton Trans.*, 2022, **51**, 16757–16763.
53 M. U. Dumesso, W. Xiao, G. Zheng, E. T. Basore, M. Tang, X. Liu and J. Qiu, *Adv. Opt. Mater.*, 2022, **10**, 2200676.
54 Y. Wang, Z. Wang, G. Wei, Y. Yang, S. He, J. Li, Y. Shi, R. Li, J. Zhang and P. Li, *Chem. Eng. J.*, 2022, **437**, 135346.
55 L. Fang, L. Zhang, H. Wu, H. Wu, G. Pan, Z. Hao, F. Liu and J. Zhang, *Inorg. Chem.*, 2022, **61**, 8815–8822.